Electronic Supplementary Material (ESI) for New Journal of Chemistry.
This journal is © The Royal Society of Chemistry and the Centre National de la Recherche Scientifique 2023

Supporting information

$Cu_3(OH)_2V_2O_7 \cdot 2H_2O$@rGO with bimetallic redox activity as a novel cathode material for calcium-ion batteries

Xingnian Tan,[a,#] Junjun Wang,[a,#] Shuhan Jin,[a] Yu Wang,[a] Fan Qiao,[a] Lei Zhang,[a] and Qinyou An*[a,b]

[a] State Key Laboratory of Advanced Technology for Materials Synthesis and Processing, Wuhan University of Technology,Wuhan 430070, China.

[b] Hubei Longzhong Laboratory, Wuhan University of Technology (Xiangyang Demonstration Zone), Xiangyang 441000, Hubei, China

[#] X.T. and J.W. contributed equally to this work.

Experimental section

Preparation of material

The CVO@rGO was prepared by the co-precipitation reaction. Firstly, 4 mmol of NH_4VO_3 (0.468g) was add to 80 mL ultra-pure water and stirred 15 min in 80 °C till complete dissolution. After the solution cooled to room temperature naturally. The above yellow solution is labeled solution A. Secondly, 30 ml 0.02g ml^{-1} graphene oxide dispersion and 6 mmol of $Cu(NO_3)_2 \cdot 2H_2O$ (1.450g) was add to 50 mL ultra-pure water and stirred 15 min till complete dissolution. The above black solution is labeled solution B. Thirdly, solution B was string rapidly while solution A was slowly added dropwise to solution B and kept string for 5 h. Finally, the above black precipitate was centrifuged and washed with deionized water for three times and absolute ethanol for three times, respectively. The obtained black product was dried in a vacuum drying oven at

60 °C for 12 hours, which was marked as CVO@rGO. For comparison, pure CVO nanoparticles were synthesized via a similar co-precipitation method, except for the addition of graphene oxide dispersion. It is worth emphasizing that the synthesis method of CVO@rGO with simple procedure and mild reaction conditions is in accord with the idea of green chemistry.

Materials characterization

In-situ XRD measurement was performed using a Bruker AXS D8 Advance powder X-ray diffractometer with an area detector using Cu Kα X-ray source. Ex situ and powder XRD measurement was performed using a Bruker AXS D2 Advance powder X-ray diffractometer with a detector using Cu Kα X-ray source. A field emission scanning electron microscope (FESEM) (JEOL-7100F) was utilized to observe the morphology of the prepared materials. Transmission electron microscope (TEM) images and high angular annular dark field scanning transmitted electron microscope (HAADF-STEM) images were obtained by utilizing JEM-2100F/Titan G2 60–300 transmission electron microscope. The VG Multi Lab 2000 instrument was used to collect X-ray photoelectron spectroscopic (XPS) spectra. Raman characterizations were measured with 532 nm wavelength using LABRAM HR Evolution Raman spectrometer. Thermogravimetric analysis (TGA) was carried out on a NETZSCH-STA449F5 thermo-analyzer with a heating rate of 10 °C min^{-1} and air atmosphere.

Electrochemical tests

The electrochemical performances were tested by assembling of CR2016 coin cells in an argon-filled glove box (<1 ppm of water and oxygen). Counter electrode was active carbon cloth (ACC). The separator was the Whatman glass fiber (GF/A). Aluminum foil is used as the current collector, which is stable and can avoid side reactions, such as a corrosion reaction during charge/discharge. The two $Cu_3(OH)_2V_2O_7{\cdot}2H_2O$ samples (CVO, CVO@rGO)

and 2 M $Ca(TFSI)_2$/tetraglyme (G4) were used as the working electrode and electrolyte, respectively. The working electrode was made by mixing prepared CVO or CVO@rGO samples (70 wt%), acetylene black (AB, 20 wt%) and poly(vinylidene fluoride (PVDF, 10 wt%). They were mixed and dispersed in N-methyl-2-pyrrolidinone (NMP) to form a slurry, and the slurry was cast onto Al foil and dried at 70 °C for 24 h. The galvanostatic charge/discharge measurements were tested on LAND CT2001A battery testing system in a voltage range of -2.0~1.0 V (vs. ACC). Cyclic voltammetry was tested on Autolab PGSTAT 302 N electrochemical workstation. Electrochemical impedance spectroscopy (EIS) was tested from 0.1 Hz to 1 MHz with an amplitude of 10 mV via Autolab PGSTAT 302 N.

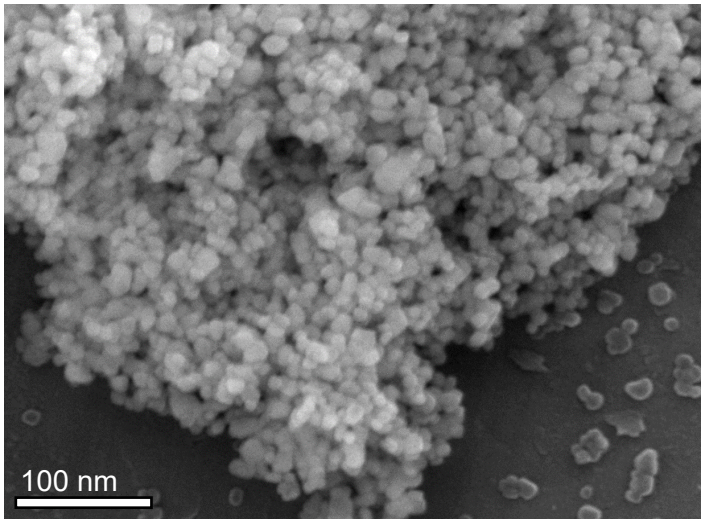

Figure S1. SEM of CVO nanoparticle.

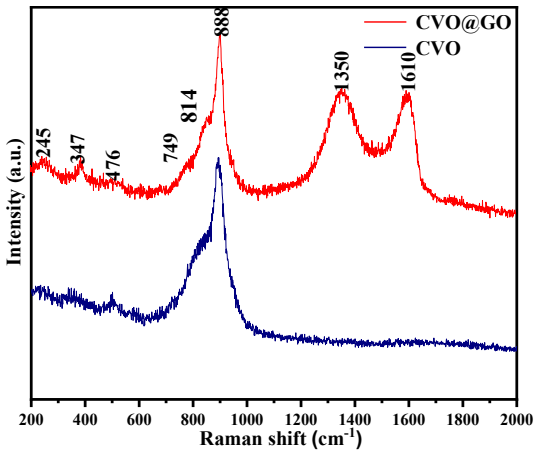

Figure S2. Raman spectra of CVO and CVO@rGO

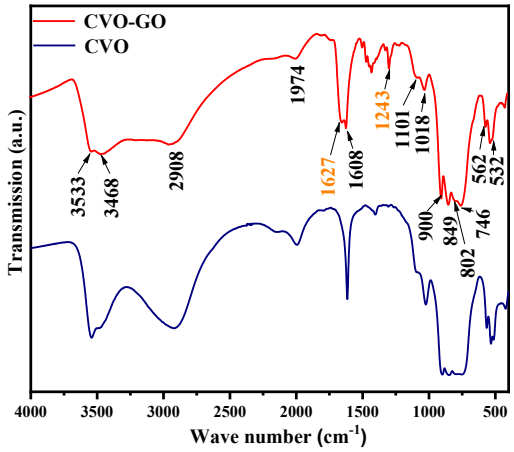

Figure S3. Fourier-transformed infrared spectrum (FT-IR) spectrum of CVO and CVO@rGO.

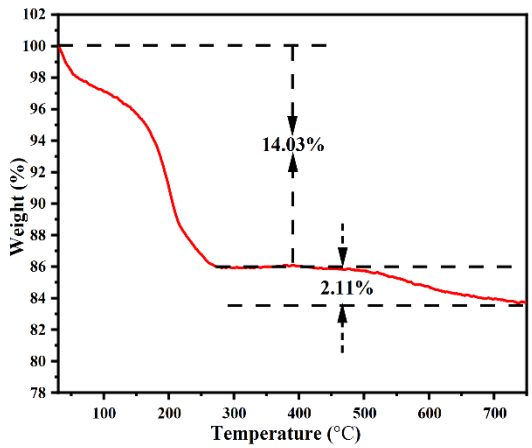

Figure S4. TGA for CVO@rGO with a heating rate of 10 °C min^{-1} and air atmosphere.

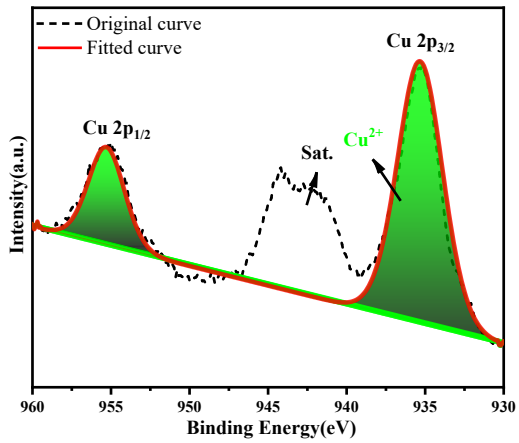

Figure S5. The XPS spectra of Cu 2p for CVO.

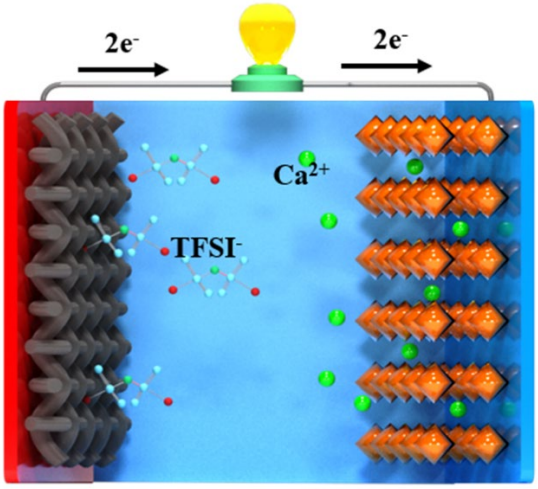

Figure S6. Configuration and working mechanism of a CVO@rGO‖2 M $Ca(TFSI)_2$/G4‖activated carbon cloth (ACC) battery with an activated carbon counter electrode for the adsorption/desorption of $TFSI^-$ and CVO@rGO working electrode that can insertion/extraction Ca^{2+}.

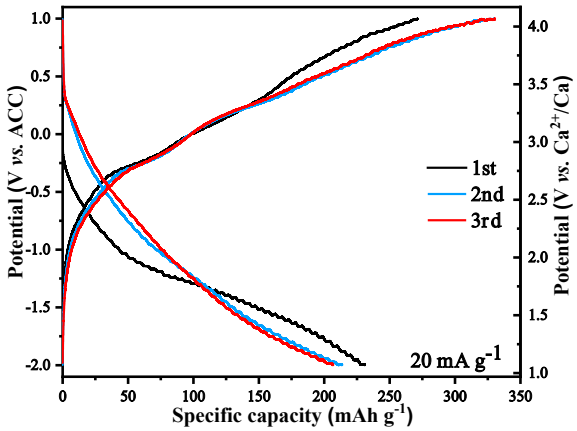

Figure S7. Galvanostatic charge/discharge profiles of CVO@rGO at first three cycles at 20 mA g^{-1} in 0.3 M $Ca(TFSI)_2$/G4 electrolyte

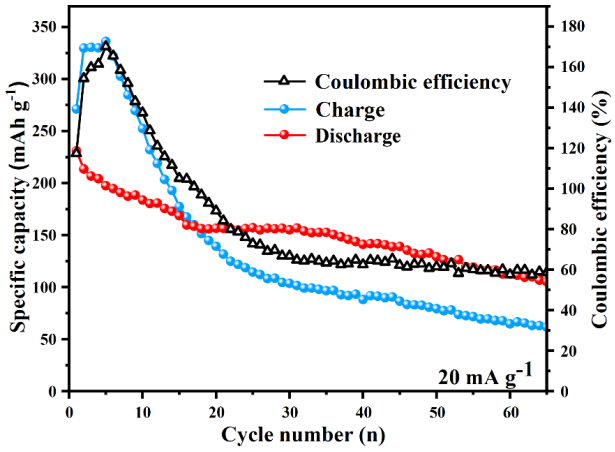

Figure S8. Cycling performances of CVO@rGO electrode at 20 mA g^{-1} in 0.3 M $Ca(TFSI)_2$/G4 electrolyte

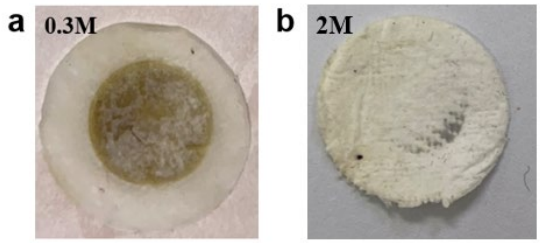

Figure S9. The photograph of separator form disassembled coin cell with (a) 0.3 M $Ca(TFSI)_2$/G4 and (b) 2 M $Ca(TFSI)_2$/G4 after 50 cycles.

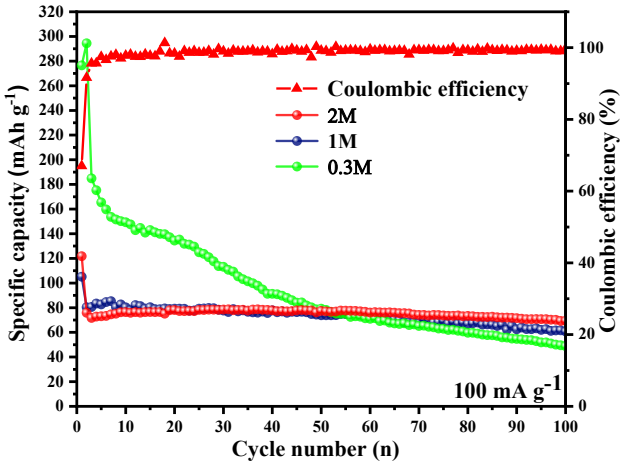

Figure S10. Cycling performances of CVO@rGO in different electrolyte concentrations at 100 mA g^{-1}.

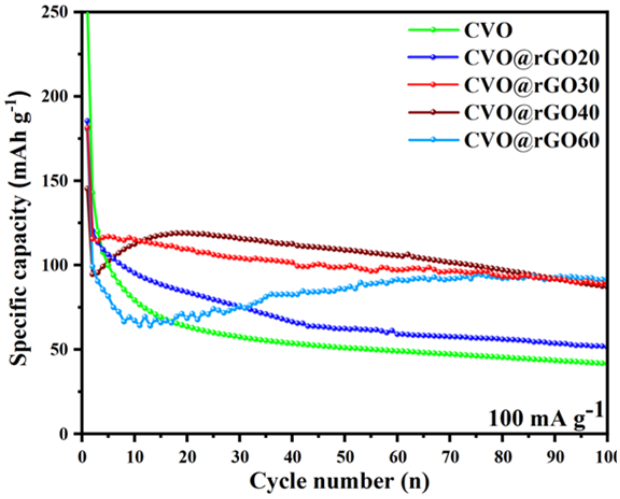

Figure S11. Cycling performances of CVO@rGO at 100 mA g^{-1} at different compound ratios.

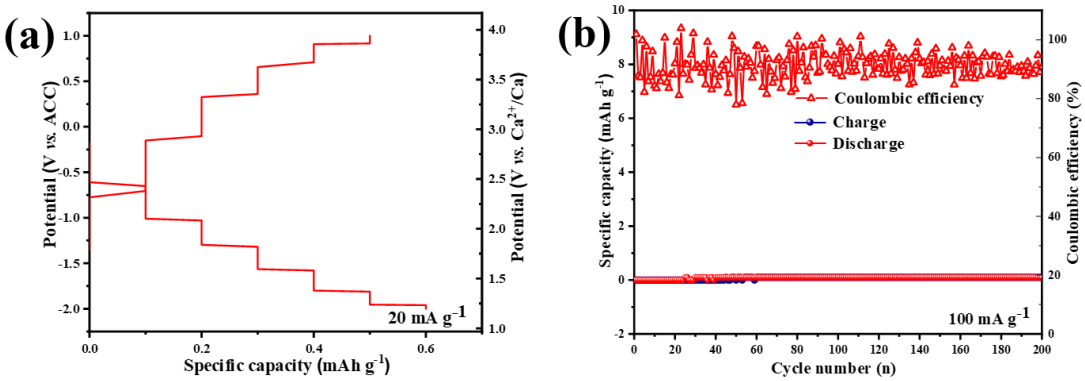

Figure S12. (a) Galvanostatic charge/discharge profiles of rGO at 20 mA g^{-1} in 2 M $Ca(TFSI)_2$/G4 electrolyte and (b) cycling performances of at 20 mA g^{-1}.

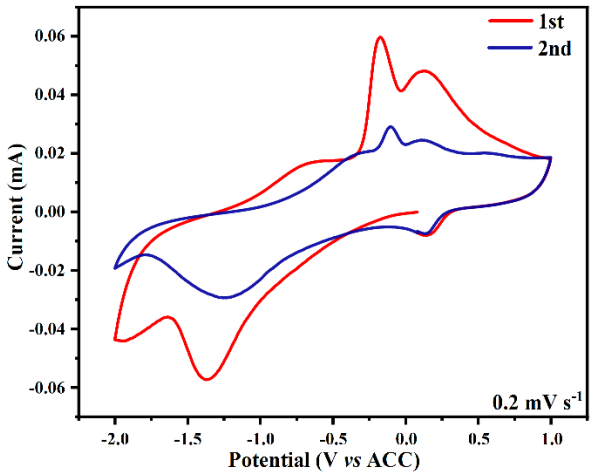

Figure S13. CV curves of CVO at a scan rate of 0.2 mV s^{-1}.

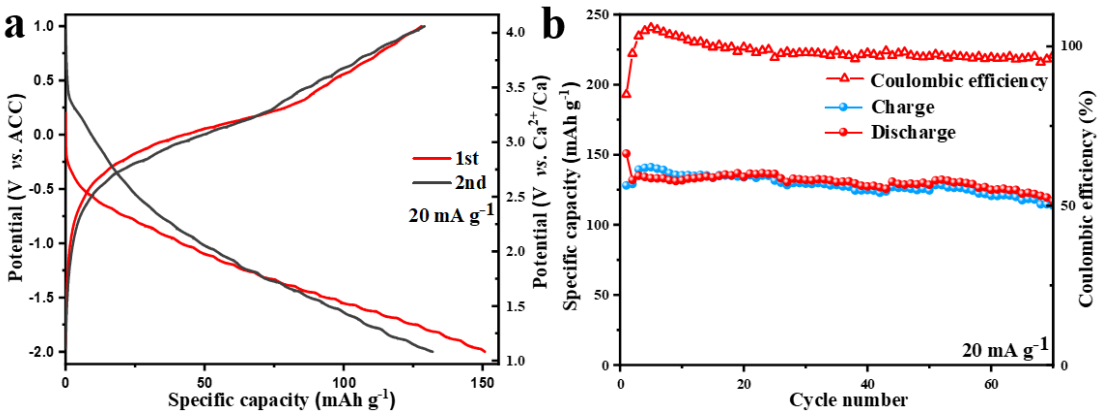

Figure S14. (a) Galvanostatic charge/discharge profiles of CVO@rGO at 20 mA g^{-1} in 2 M $Ca(TFSI)_2$/G4 electrolyte and (b) cycling performances of at 20 mA g^{-1}.

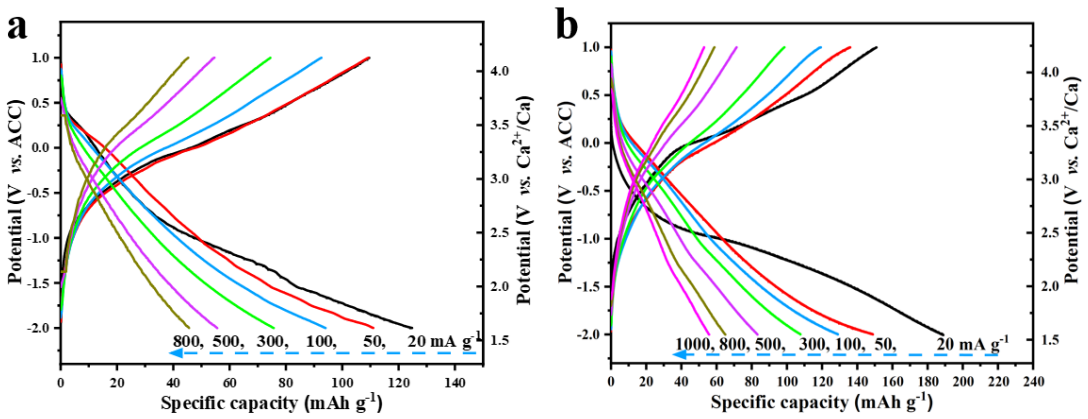

Figure S15. Charge and discharge profiles of CVO@rGO at different current densities, (a) at room temperature and (b) at 50 °C.

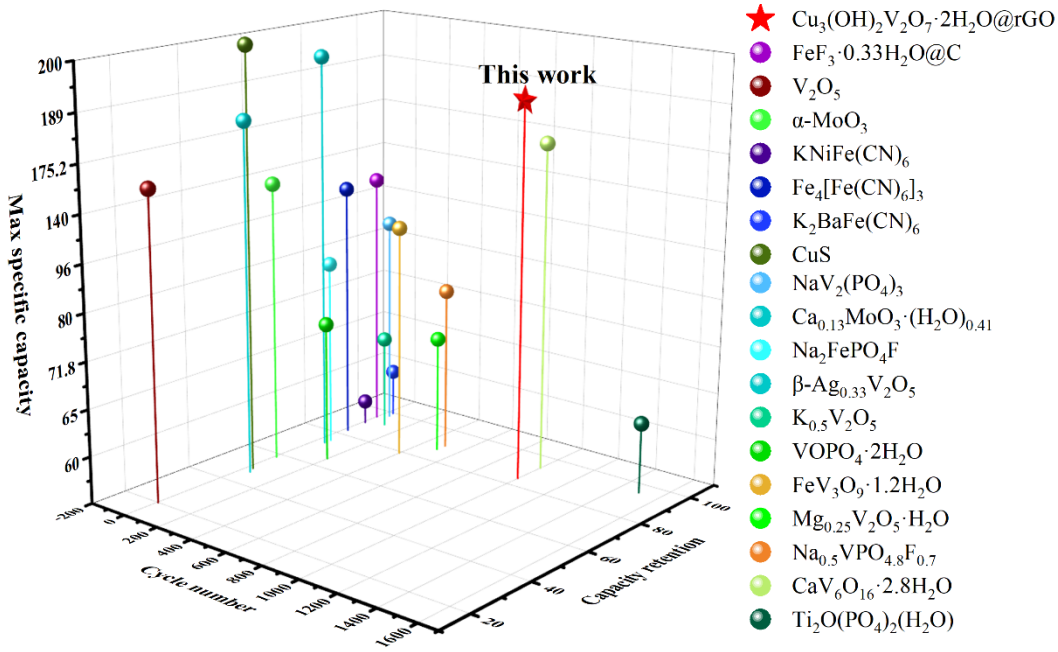

Figure S16. Performance comparison between CVO@rGO and other Cathode materials for Ca-ion batteries.

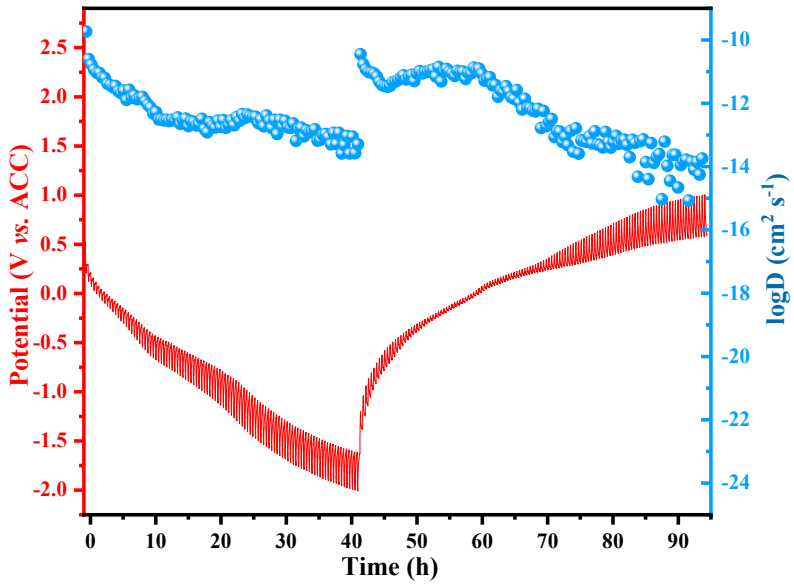

Figure S17. GITT curve of CVO electrode and diffusivity of one cycle.

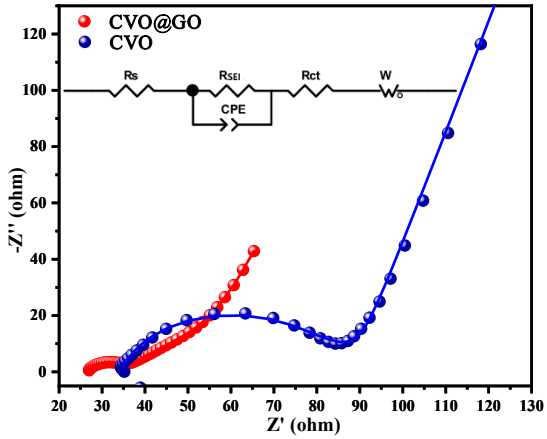

Figure S18. The Electrochemical impedance spectroscopy (EIS) results of CVO and CVO@rGO

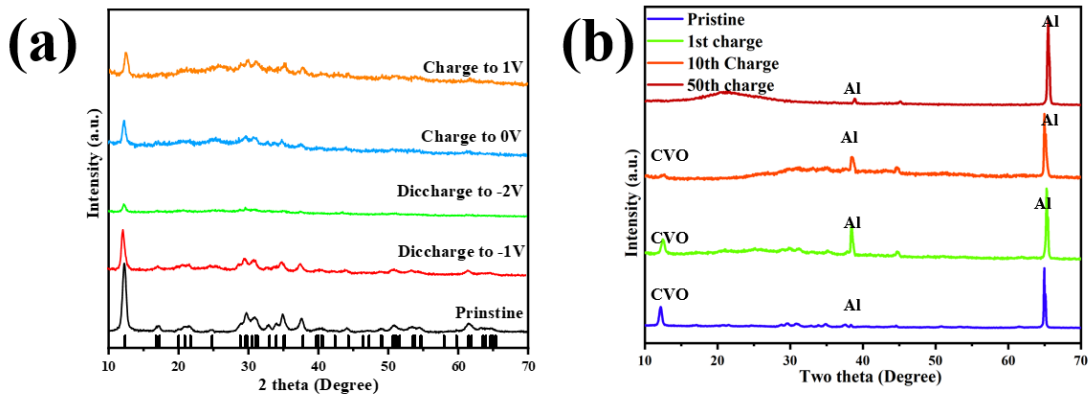

Figure S19. (a)*Ex-situ* XRD patterns for CVO@rGO at different states. (b) *Ex-situ* XRD patterns for charged CVO@rGO at different cycle

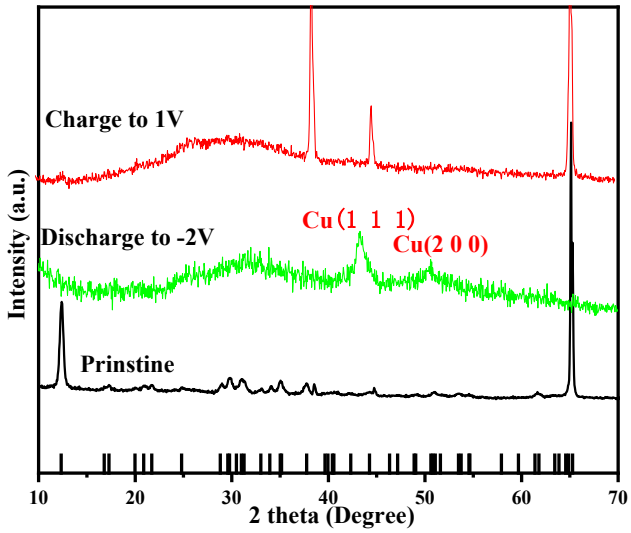

Figure S20. *Ex-situ* XRD patterns for CVO at different states.

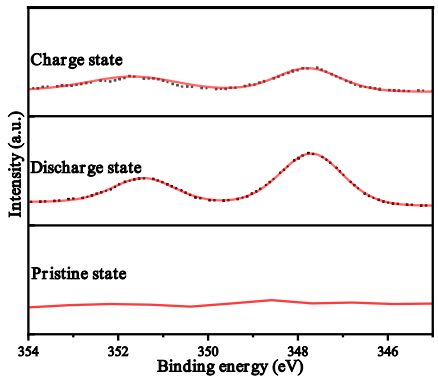

Figure S21. *Ex-situ* XPS spectra of Ca 2p at different states for CVO@rGO electrode.

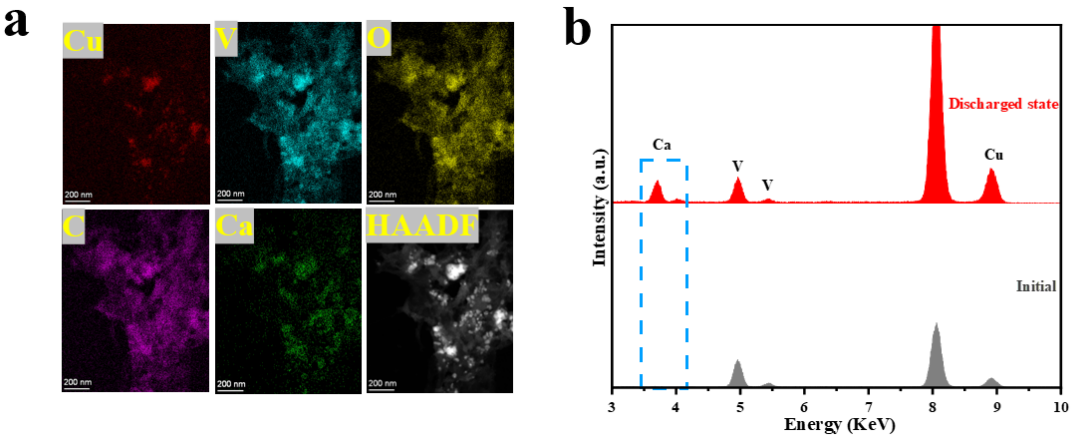

Figure S22. (a) HAADF image and corresponding elemental maps at discharged states. (b) EDX spectra of CVO@rGO at initial and discharged states.

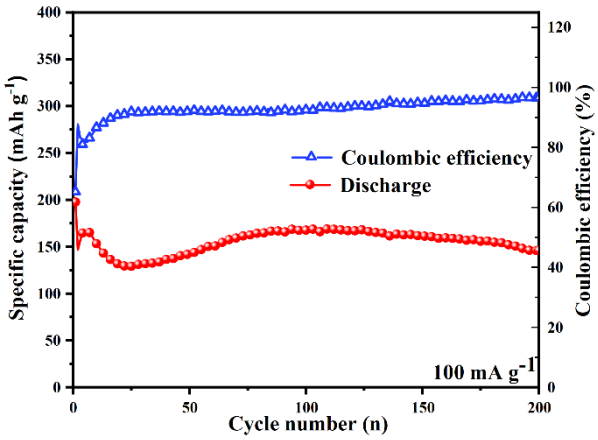

Figure S23. Cycling performances of CVO@rGO at 100 mA g^{-1} in 0.5 M $Ca(TFSI)_2$/AN electrolyte.

Table S1. The EIS fitted result of CVO

Element	Freedom	Value	Error	Error%
Rs	Free(?	-3366	4.75E+05	14125
Rsei	Free(+)	6.747	0.30757	4.5586
CPE-T	Free(?	6.50E-06	1.17E-06	18.003
CPE-P	Free(+)	0.85342	0.019717	2.3104
Rct	Free(+)	3392	4.75E+05	14017
W1-R	Free(+)	1.045	2.6281	251.49
W1-T	Free(+)	4.40E-06	2.64E-05	600.34
W1-P	Free(+)	0.21948	0.002172	0.98943

Table S2. The EIS fitted result of CVO@rGO

Element	Freedom	Value	Error	Error%
Rs	Free(?	-6.35E+10	5.20E+06	0.00819
Rsei	Free(+)	44.26	0.077906	0.17602
CPE-T	Free(?	4.28E-06	4.20E-09	0.098074
CPE-P	Free(+)	0.85659	0.000577	0.067352
Rct	Free(+)	6.35E+10	5.20E+06	0.00819
W1-R	Free(+)	31.59	1.6961	5.3691
W1-T	Free(+)	0.009437	0.000694	7.3489
W1-P	Free(+)	0.42144	0.002721	0.64564

Table S3. The quantitative elemental ratios of CVO@rGO at initial state.

Z	Element	Atomic Fraction (%)	Mass Fraction (%)
6	C	68.93	36.88
8	O	11.58	8.53
20	Ca	0	0
23	V	1.03	2.35
29	Cu	18.45	52.24

Table S4. The quantitative elemental ratios of CVO@rGO at discharged state.

Z	Element	Atomic Fraction (%)	Mass Fraction (%)
6	C	66.16	35.43
8	O	13.77	9.83
20	Ca	1.26	2.25
23	V	1.46	3.32
29	Cu	17.35	49.16

Table S5. Performance comparison between CVO@rGO and other Cathode materials for Ca-ion batteries.

Material	Counter Electrode/Reference Electrode	Capacity (mAh/g)/current density (mA/g)	Number of cycles	Capacity retention	references
$Cu_3(OH)_2V_2O_7 \cdot 2H_2O$@rGO	ACC/-	189.9/20 55.4/1000	1000	84.2	This work

$CaV_6O_{16}\cdot 2.8H_2O$	ACC/-	175.2/50 69/500	100 1000	74.7 93	[1]
$Mg_{0.25}V_2O_5\cdot H_2O$	ACC/-	70.0/100	500	86.9	[2]
$K_2BaFe(CN)_6$	Carbon paper/Ag-Ag^+	60.0/12.5	30	96.6	[3]
Na_2FePO_4F	BP2000 carbon/-	80/10	50	75	[4]
α -MoO_3	Activated carbon/Ca	140/20	12	58	[5]
V_2O_5	Activated carbon/Ag-Ag^+	150/50	5	20	[6]
$Fe_4[Fe(CN)_6]_3$	Graphite rod/Ag-Ag+	120/125	80	83	[7]
$KNiFe(CN)_6$	AC/Ag-Ag^+	45/25	12	90	[8]
CuS	ACC/-	200/100	30	49	[9]
$FeF_3\cdot 0.33H_2O$@C	AC/Ag-Ag^+	120/50	3	95	[10]
$NaV_2(PO_4)_3$	AC/-	81/3.5	40	97.6	[11]
$Ca_{0.13}MoO_3\cdot(H_2O)_{0.41}$	AC/-	192/85.65	50	72.8	[12]
$VOPO_4\cdot 2H_2O$	ACC/-	71.8/100	200	65	[13]
$Na_{0.5}VPO_{4.8}F_{0.7}$	AC/-	75/50	500	90	[14]
$K_{0.5}V_2O_5$	AC/-	65/66.6	100	92	[15]
$FeV_3O_9\cdot 1.2H_2O$	AC/-	96/200	400	79	[16]

β -$Ag_{0.33}V_2O_5$	AC/-	179/12.3	50	47	[17]
$Ti_2O(PO_4)_2(H_2O)$	AC/-	60.8/50	1500	95	[18]

Reference

1. Wang, J.; Wang, J.; Jiang, Y.; Xiong, F.; Tan, S.; Qiao, F.; Chen, J.; An, Q.; Mai, L. Adv. Funct. Mater., 2022, 2113030.
2. X. Xu, M. Duan, Y. Yue, Q. Li, X. Zhang, L. Wu, P. Wu, B. Song and L. Mai, ACS Energy Lett, 2019, 4, 1328-1335.
3. Padigi, P.; Goncher, G.; Evans, D.; Solanki, R., J. Power Sources 2015, 273, 460-464.
4. Lipson, A. L.; Kim, S.; Pan, B.; Liao, C.; Fister, T. T.; Ingram, B. J., J. Power Sources 2017, 369, 133-137.
5. Cabello, M.; Nacimiento, F.; Alcántara, R.; Lavela, P.; Pérez Vicente, C.; Tirado, J. L., Chem. Mater. 2018, 30 (17), 5853-5861.
6. Murata, Y.; Takada, S.; Obata, T.; Tojo, T.; Inada, R.; Sakurai, Electrochim. Acta, 2019, 294, 210-216.
7. Kuperman, N.; Padigi, P.; Goncher, G.; Evans, D.; Thiebes, J.; Solanki, Jenny Stanford Publishing, 2017, 342, 414-418.
8. Tojo, T.; Sugiura, Y.; Inada, R.; Sakurai, Y. J. Electrochim. Acta, 2016, 207, 22-27.
9. Ren, W.; Xiong, F.; Fan, Y.; Xiong, Y.; Jian, Z. J. ACS Appl. Mater. Inter-faces, 2020, 12 (9), 10471-10478.
10. Murata, Y.; Minami, R.; Takada, S.; Aoyanagi, K.; Tojo, T.; Inada, R.; Sakurai, Y, AIP Conf. Proc, AIP Publishing LLC: 2017; p 020005.
11. Kim, S.; Yin, L.; Lee, M. H.; Parajuli, P.; Blanc, L.; Fister, T. T.; Park, H.; Kwon, B. J.; Ingram, B. J.; Zapol, ACS Energy Lett, 2020, 5 (10), 3203-3211.
12. Chae, M. S.; Kwak, H. H.; Hong, S.-T. J. A. Adv. Energy Mater, 2020, 3 (6), 5107-5112.
13. J. Wang, S. Tan, F. Xiong, R. Yu, P. Wu, L. Cui and Q. J. An, *Chem. Commun*., 2020, **56**, 3805-3808.
14. Xu, Z.-L.; Park, J.; Wang, J.; Moon, H.; Yoon, G.; Lim, J.; Ko, Y.-J.; Cho, S.-P.; Lee, S.-Y.; Kang, K. J. Nat. Commun., 2021, 12 (1), 3369.
15. Purbarani, M. E.; Hyoung, J.; Hong, S.-T. J. A. Adv. Energy Mater., 2021, 4 (8), 7487-7491.
16. Chae, M. S.; Setiawan, D.; Kim, H. J.; Hong, S. Batteries, 2021, 7 (3), 54.
17. Hyoung, J.; Heo, J. W.; Jeon, B.; Hong, S.-T. J. Mater. Chem. A., 2021, 9 (36), 20776-20782.
18. Prabakar, S. R.; Park, W.-B.; Seo, J. Y.; Singh, S. P.; Ahn, D.; Sohn, K.-S.; Pyo, M. J. Energy Storage Materials, 2021, 43, 85-96.